Turkish Journal of Physics

http://journals.tubitak.gov.tr/physics/

Research Article

Turk J Phys
(2018) 42: 415 – 424
© TÜBİTAK
doi:10.3906/fiz-1803-12

Mapping heavy elements in the supernova remnant G290.1-0.8

Murat HÜDAVERDİ*
Department of Physics, Faculty of Science and Art, Yıldız Technical University, Turkey

Received: 12.03.2018 • **Accepted/Published Online:** 09.07.2018 • **Final Version:** 15.08.2018

Abstract: We present the imaging and spectroscopic study results of G290.1-0.8 Supernova Remnant (SNR) using the Suzaku X-ray archival data. The SNR belongs to the mixed-morphology class with its centrally peaked asymmetric X-ray core and distorted radio shell-like plasma. The X-ray spectra is well defined with isothermal plasma of $kT_e \sim 0.5$ keV. The radial profile shows enhanced elemental abundances. The EW maps reveal inhomogeneous asymmetric spatial distribution of elemental abundances. The northeast of the SNR is bright in Ne, Mg, and Si. The EW maps are enhanced in the direction of the X-ray elongation, suggesting that the distorted X-ray structure is dominated by a core-collapse $20 \sim 25$ $M_\odot$ progenitor star ejecta.

Key words: Supernova remnants, X-rays, gamma-rays, interstellar medium

1. Introduction

Supernova remnants (SNRs) are structures that result from the explosive end of massive stars. Heavy elements are produced and spread into the interstellar medium by these cosmic laboratories. Based mainly on their radio morphology, SNRs have been classified as shell-type and crab-type. A different type of morphology is also observed as crab-like at the center and shell-type on the outside [1]. These mixed-morphology SNRs such as W44, W28, and 3C391 have center-filled thermal X-ray and shell-like radio morphologies [2].

G290.1-0.8 is one of the mixed-morphology galactic SNRs [3]. It was first discovered in a radio sources survey by Mills, Slee, and Hill [4] and named after their initials as MSH 11-61A. This radio SNR was identified by a faint smooth ring as optical counterpart by CTIO (Cerro Tololo Inter-American Observatory) 4m telescope [5]. Following the radio observations at 408 MHz [6] and 5–8 GHz [7], the SNR was classified as shell-type with an angular size of 15×10 arcmin^2. The Australia Telescope Compact Array (ATCA) H I line and 20 cm radio continuum observations showed the complex gas distribution and the dynamics of G290.1-0.8 [8]. G290.1-0.8 was first studied in X-rays at the Einstein Observatory as part of an SNR survey [9]. A centrally bright morphology was reported in the study. Later, Slane et al. [3] analyzed The Advanced Satellite for Cosmology and Astrophysics (ASCA) Observatory GIS data and showed that the X-ray emission was of thermal nature and classified the remnant as a mixed-morphology SNR. The XMM-Newton and Chandra analysis results emphasized the asymmetrical structure of G290.1-0.8 [10]. They also reported that the SNR was formed by a core collapse of a high-mass progenitor with a bipolar wind. Suzaku data analysis results demonstrated that the center and the northwest of the SNR plasma was recombining, while the other parts of it were ionizing [11].

*Correspondence: hudaverd@yildiz.edu.tr

A further multiwavelength study of gamma-ray and Fermi-LAT Suzaku X-ray showed that the γ-ray emission was hadronic in nature and the X-ray emission was coming from the shock-heated plasma [12]. Although the morphology is well defined and there are no G290.1-0.8 data that have not been virtually untouched, no elemental abundance distribution map had been conducted for the SNR so far. Therefore, we had a strong motivation to search for the spatial profile for the metals within the G290.1-0.8 plasma in order to understand the ejecta geometry and the relations between γ-ray/X-ray/radio plasma.

In this paper, we aimed to investigate the spatial distribution of elemental abundances of G290.1-0.8 using the equivalent width mapping technique [13]. For this purpose, we used the archival Suzaku data, which had a good energy resolution for our study. We also revisited the GeV γ-ray properties of G290.1-0.8 using the Fermi-LAT data. The observations and data reduction steps are described progressively. In Sections 2 and 3, gamma-ray and X-ray analysis results are reported in detail. In Section 4, the equivalent width maps are explained. We discuss the nature of the ejecta and the elemental abundance distributions in Section 5.

2. Gamma-ray analysis

The large effective area and wide field of view of the Large Area Telescope on board the Fermi Gamma Ray Space Telescope (Fermi-LAT) [14] allow the detection and analysis of the gamma-ray emission from pulsars or pulsar wind nebulae. We used the archival data from 4 August 2008 to 16 December 2011. Using `gtselect` of the Fermi Science Tools (FST) analysis package 2, we selected photons of energies greater than 200 MeV with a zenith angle less than 105° cut to remove contaminations from the Earth's limb.

In Figure 1, we generated a 5.5° × 2.5° γ-ray count map in units of counts degree^{-2} centered at

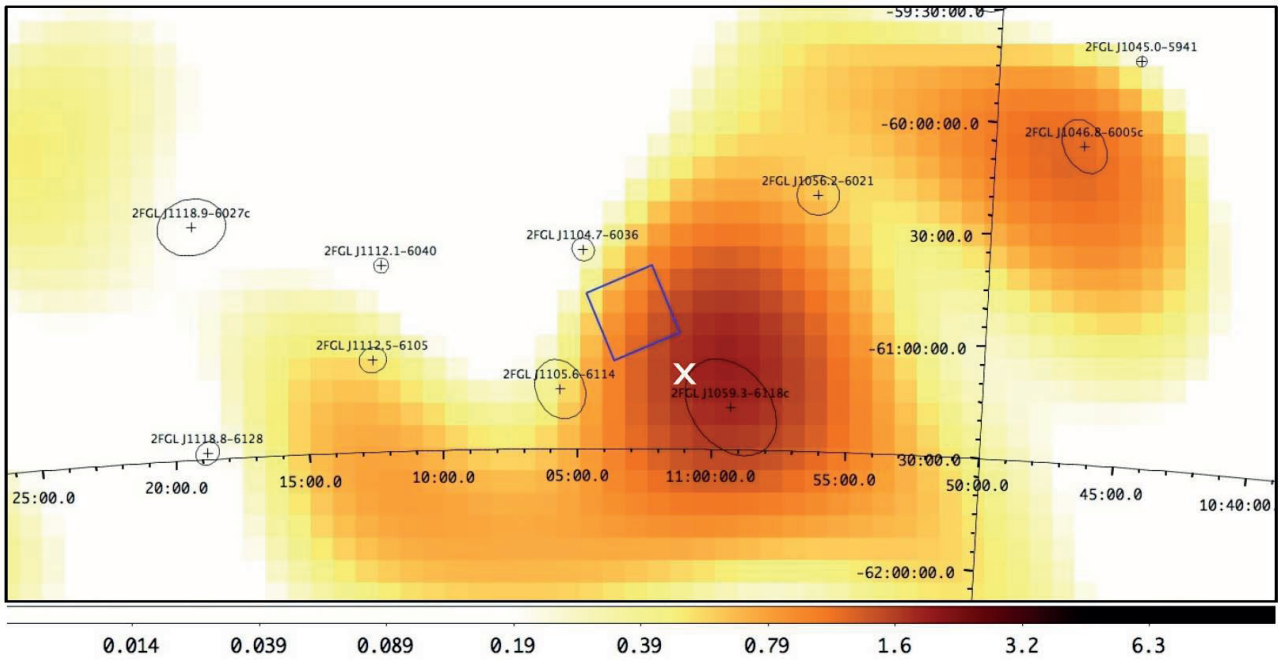

Figure 1. The Fermi-Lat map at the 2 − 200 GeV γ-ray emission around G290.1-0.8. The labeled crosses and circles (or ellipses) correspond to the positions and errors of the Fermi-Lat sources, respectively. The white X corresponds to the position of ICG J11014-6103 neutron star [15]. The tilted box at the center shows the SUZAKU XIS chip field of view for G290.1-0.8 observation.

$l = 166°.0$, $b = -60°.8$ around the SNR. The crosses and the ellipses indicate the positions of the Fermi-LAT sources and associated errors, respectively. The tilted square at the center represents the Suzaku field of view for G290.1-0.8 observation. The location of ICG J11014-6103 is plotted as the white X, which is a supersonically traveling neutron star [15]. There is no detected neutron star associated with the SNR in the literature, and ICG J11014-6103 is a bit far ($\sim$10 arcmin) to relate clearly. The image was adaptively smoothed in order to highlight the γ-ray emission in the vicinity. It is clearly seen that G290.1-0.8 is located in a very complicated portion of the γ-ray sky. The number of the Fermi-LAT sources around the SNR is noticeably high. The three sources 2FGL J1104.7-6036, 2FGL J1105.6-6114, and 2FGL J1059.3-6118c are exceptionally close to G290.1-0.8, within the vicinity of $\sim 1°$ distance. There is no evident physical relation between the Fermi-LAT sources and G290.1-0.8 as also noted in the previous studies [16].

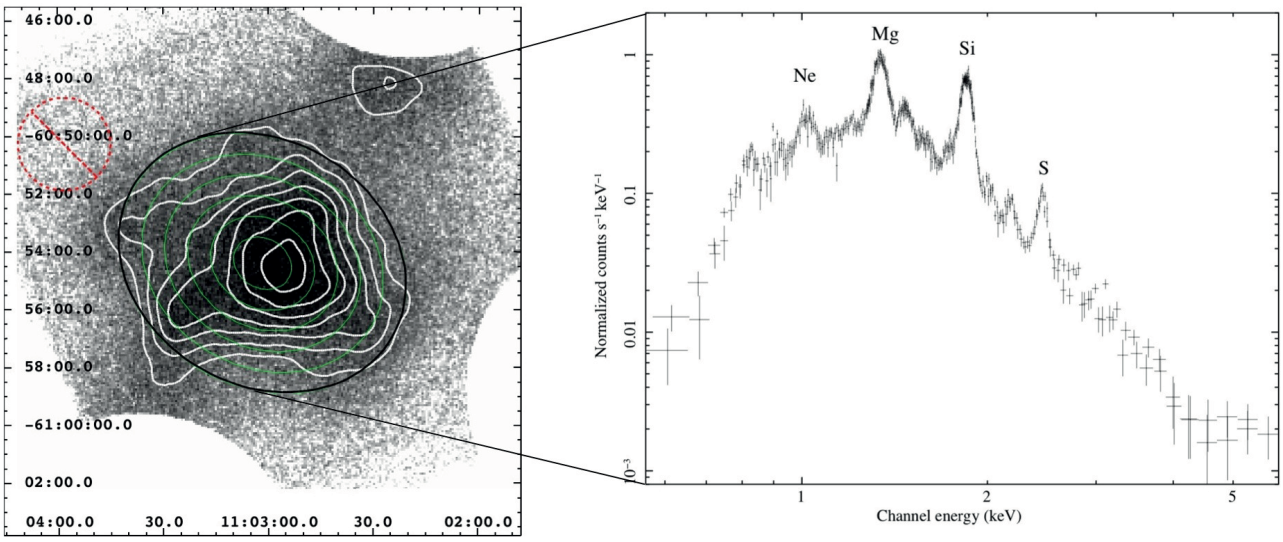

Figure 2. Left: The composite raw image was constructed using the data from XIS0, XIS1, and XIS3 in $0.3-10$ keV energy band. The image corners were masked due to irradiation of the ^{55}Fe calibration source. In order to highlight the X-ray features, the contours were plotted after being smoothed by a Gaussian kernel of $\sigma = 10$ pixels and logarithmically spaced by a factor of 1.4, starting from 23.2 counts cm^{-2} s^{-1}. The regions of source and background for spectral analysis are indicated with elliptical annulus and dashed red circle, respectively. Right: Suzaku FI-XIS chip spectrum of G290.1-0.8 plotted against energy of 0.5-6 keV. The prominent lines are Ne, Mg, Si and S, as noted.

3. Data analysis

3.1. Observation and data reduction

We downloaded the Suzaku archival data of G290.1-0.8 from the Data Archives and Transmission System (DARTS)[1]. The SNR was observed on 25 June 2011 for 110.6 ksec with the X-ray Imaging Spectrometer (XIS) [17] detectors on Suzaku. The XIS is composed of four CCD cameras: XIS0, XIS2, and XIS3 have front-illuminated (FI) sensors and XIS1 has a back-illuminated (BI) sensor. The entire imaging area of the XIS2 was lost in 2006 November[2] because of the damage by a possible micrometeorite. Therefore, we used XIS0, XIS1, and XIS3 throughout the analysis. HEAsoft tools version 6.18 was used for the data reduction and analysis. We reprocessed the archival data with CALDB 4.6.7 calibration database. For extracting the images and spectra,

[1] http://www.darts.isas.jaxa.jp/astro/suzaku/
[2] http://www.astro.isas.jaxa.jp/suzaku/news/2006/1123/

we used `Xselect` version 2.4c. We combined 3×3 and 5×5 event files using `xis5x5to3x3` and version 2.4c of `Xselect`.

3.2. X-ray imaging analysis

We show the raw XIS mosaic image of G290.1-0.8 in the 0.3–10.0 keV band in Figure 2, left panel. The corner of the CCD chip illuminated by the ^{55}Fe calibration source is excluded from the image as seen by clippings. In order the highlight the plasma emission, we overlaid the contour levels after smoothing by a $\sigma=10$ Gaussian kernel. The contours are logarithmically spaced by a factor of 1.4, starting from 23.2 counts cm^{-2} s^{-1}. It is evident that the plasma emission is center-filled with X-ray, which is elongated in the NW-SE direction in the outskirts. Thus, we extracted the source spectrum from an elliptical rather than a circular region. The radial profile is also defined by five elliptical–annular rings (in green). The dashed red circle at the left corner with 1.7 arcmin represents the background region. Background-subtracted source XIS spectra in the 0.5–6 keV is shown in Figure 2, right panel. The strong prominent lines are Ne, Mg, Si, and S, as clearly seen.

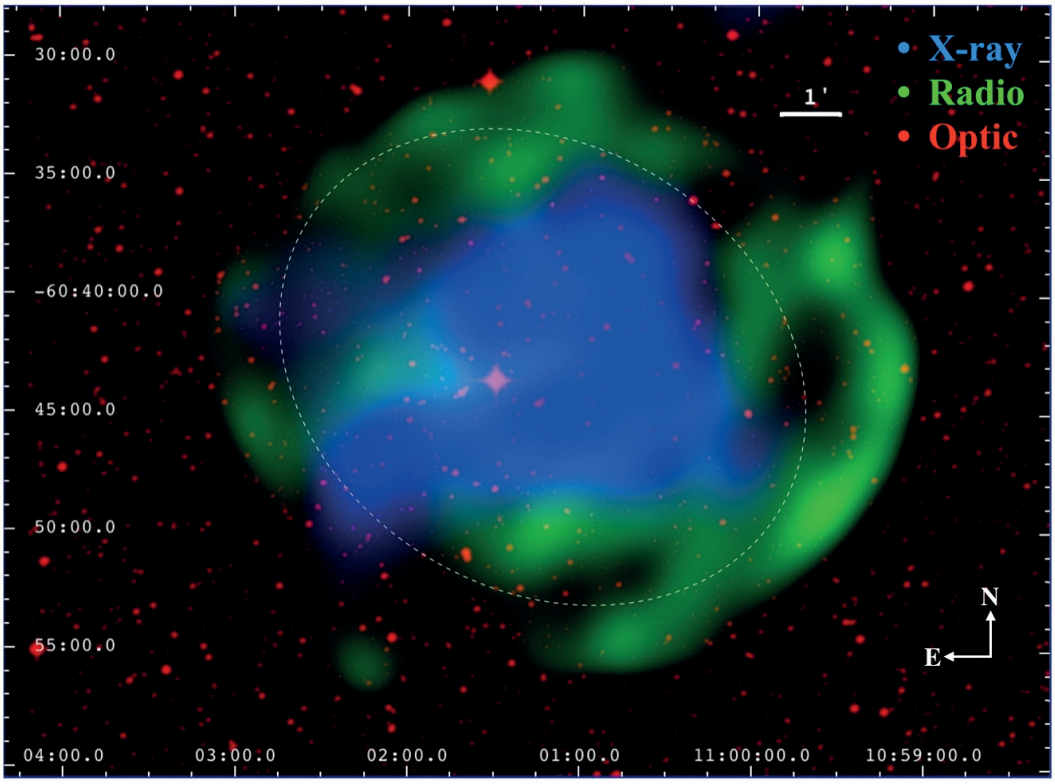

Figure 3. The composite image of G290.1-0.8 shows the distribution of the optical image (from the DSS) in red, radio emission (from the MOST) in green, and the extended X-ray plasma (from Suzaku) in blue. The spectra extracted region is shown with the dotted ellipse.

To determine any possible relation between different wavelength emissions from the SNR field, we also generated a three-color RGB image by using the optical image in red, radio image in blue, and X-ray band image in red, as shown in Figure 3. The dotted elliptical region for the source spectrum was added for visual aid. The image is approximately 18 arcmin $\times$ 13 arcmin and the white line shows the 1 arcmin scale on the image. The optical image is from the Digitized Sky Survey (DSS), which was obtained online from the

Anglo–Australian Observatory[3]. The shell-like green radio morphology of the remnant is from The Molonglo Observatory Synthesis Telescope (MOST)[4] at 843 MHz [18]. The blue X-ray image fills the center of the SNR. There is no definite optical source related with the structure. The three-color RGB image clearly shows the mixed-morphology with center-filled X-ray plasma (blue) and radio shell (green).

3.3. Spectral analysis

In the spectral analysis, we used `Xselect` to extract the source and background photon counts. For each region, we created a redistribution matrix and effective area files using the tasks `xisrmfgen` and `xissimarfgen`, respectively [19]. The spectral modeling was performed by `Xspec` version 12.9.0 [20]. We adopted the solar abundances of Wilms, Allen, and McCray [21]. Throughout the present study, all uncertainties correspond to the 90% confidence level.

The background (BG) photons were extracted from a circular source-free region at the corner chip. The BG emission was modeled, and then a fake BG file was created by `fakeit` in `Xspec` to be used in the source spectral analysis. The overall BG model includes the Galactic ridge X-ray emission (GRXE), foreground thermal emissions (FE), and the cosmic X-ray background (CXB) (see e.g. [22] and the references therein). Since G290.1-0.8 covers a large portion of the XIS FoV, the BG photons were extracted from a nearby blank X-ray pulsar 1E1048.1–5937 region in a similar study [11]. The local BG model parameters in our work are consistent with those reported in [11]; GRXE spectra as the sum of high-temperature plasma (HP $kT \sim$7 keV) and low-temperature plasma (LP $kT \sim$1 keV), FE optically thin thermal plasma ($kT \leq$1 keV), and CXB power-law (Γ=1.4). Thus, we applied the BG model as described extensively in [11].

G290.1-0.8 diffuse plasma emissions were fitted into various models: VMEKAL, VNEI, VPSHOCK, and VRNEI, each modified by a galactic absorption model (TBABS). Free parameters are the electron temperature, kT_e; the ionization time τ, where τ is electron density times the elapsed time after the shock heating, $n_e t$. The elemental abundances of O (=C=N), Ne, Mg, Si, and S were set as free parameters. Abundances of the other elements were fixed to the solar values. The Recombining Plasma (RP) code VRNEI model provides a substantially improved fit for annular sections yielding a reduced $\chi^2_\nu \leq$1.2 for the spectral values, which is also reported in [11]. The overall plasma in the large elliptical region (see Figure3) is modeled by both Isothermal Plasma (IP) and RP models; however, χ^2_ν values do not allow us to discriminate clearly.

Table 1. Best-fit parameters of the G290.1-0.8 spectra.

Parameters	Ellipse		Ring-1	Ring-2	Ring-3	Ring-4	Ring-5
	IP	RP	RP	RP	RP	RP	RP
$N_H(\times 10^{21} cm^{-2})$	4.66 ± 0.40	5.87 ± 0.30	7.97 ± 0.94	7.04 ± 0.59	5.66 ± 0.44	5.92 ± 0.57	5.53 ± 0.57
kT_e (keV)	0.54 ± 0.03	0.54 ± 0.05	0.53 ± 0.13	0.54 ± 0.08	0.55 ± 0.08	0.53 ± 0.09	0.55 ± 0.10
Ne	0.29 ± 0.08	0.55 ± 0.04	0.79 ± 0.22	0.45 ± 0.07	0.66 ± 0.09	0.49 ± 0.07	0.50 ± 0.08
Mg	1.00 ± 0.22	1.56 ± 0.14	1.68 ± 0.52	1.50 ± 0.24	1.89 ± 0.31	1.49 ± 0.25	1.59 ± 0.31
Si	2.01 ± 0.42	2.65 ± 0.29	2.68 ± 0.96	2.29 ± 0.44	3.38 ± 0.66	2.61 ± 0.51	2.64 ± 0.31
S	1.95 ± 0.43	2.62 ± 0.31	1.72 ± 0.67	1.87 ± 0.39	3.39 ± 0.70	2.46 ± 0.54	2.86 ± 0.70
χ^2_ν (d.o.f.)	1.18 (974)	1.16 (1142)	1.13 (293)	1.18 (497)	1.13 (601)	1.20 (596)	1.19 (612)

[3]See http://www.aao.gov.au/index.html
[4]See http://www.physics.usyd.edu.au/sifa/Main/MOST

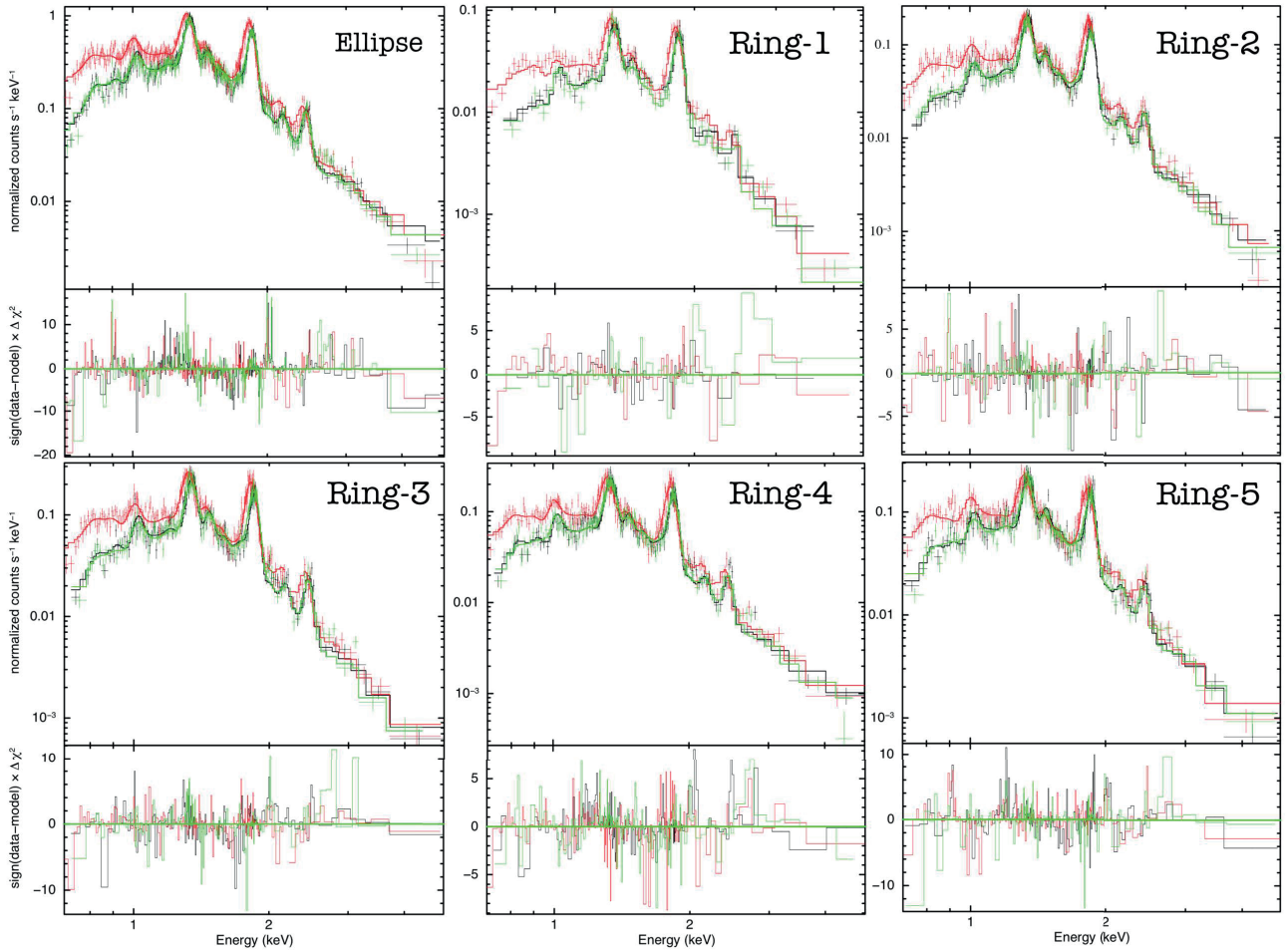

Figure 4. The X-ray spectra from G290.1-0.8 annular regions from XIS0 (black), XIS1 (red), and XIS3 (green). Histograms correspond to RP best-fit models as described in the text.

The best-fit spectra and parameters for the RP fits and IP fit (for overall Ellipse) are shown in Figure 4 and Table 1. The XIS0, XIS1, and XIS3 data were fit simultaneously in the energy range 0.7–5 keV, which are extracted from the annular rings. The spectra are well modeled with a low-temperature plasma $kT_e \sim 0.55$ keV, which does not vary much radially, and the elemental abundances are over-solar value. The radial profile of the atomic emission lines gives critical information to help understand the nucleosynthesis yield of the core-collapse progenitor stars. In Figure 5, we show the radial elemental abundance pattern for Ne, Mg, Si, and S normalized by the value of Si. The different colors represent the results from the radial rings, which are labeled as R1 to R5. The ratio of Ne/Si and Mg/Si are relatively less than S/Si. This abundance pattern is expected from a core-collapse progenitor star of M$<$30 M$_\odot$ [23]. A similar pattern was also reported for the NW region in a previous study [11]. Therefore, G290.1-0.8 elemental abundances can be described by a progenitor star nucleosynthesis yield of mass of 20$\sim$25 M$_\odot$. The radial profile analysis results give crucial information about the plasma but the spatial information of the elemental abundances is very limited. Hence, in the following section, we try to locate the prominent elements in the SNR plasma.

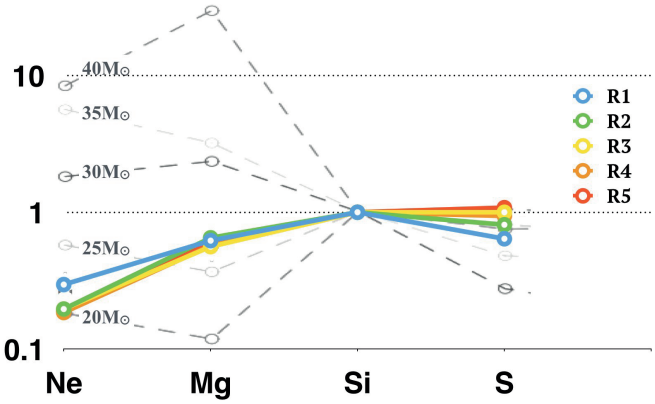

Figure 5. The radial variation of the abundance pattern for each ring normalized by the value of Si. The pattern is similar to the progenitor star nucleosynthesis yield of 20∼25 $M_{\odot}$ [23].

4. Equivalent width maps

G290.1-0.8 ejecta is a metal abundant and its X-ray spectra shows strong emission lines of heavy elements. The prominent lines are clearly seen in Figure 2, right panel. The SNR plasma is crowded with Ne Kα, Ne Heα, Ne Lyα, Mg Kα, Si Kα_1 and Si Kα_2, and S Kα_2 and S Kα_1. The energies of X-ray emission lines for these elements are given in Table 2. The emission line strengths are often given as equivalent widths (EW) [24]. The EW maps reveal complex elemental structures and implies dynamics within the SNR. The reliability of EW maps are tested in detail on the oxygen-rich SNR G292.0+1.8 from Chandra data [25].

The EW of any line feature is given by

$$EW = \int \left(\frac{I_\nu - I_\nu^\circ}{I_\nu^\circ} \right), \tag{1}$$

where I_ν is the total observed intensity including the line, and I_ν° is the continuum intensity without the line in the respective energy bands. The analysis routine for EW map construction was described in [25]. Figure 6 shows constructed EW images by selecting photons around the broad-line emissions (Table 2). The SNR spectra exhibits two broad-line features for Ne (Heα at ∼0.93 keV and Lyα at ∼1.05 keV), as also seen in a young galactic SNR G292.0+1.8. The images were created by 0.89–1.10 keV in blue, 1.20–1.49 keV in red, 1.6–2.0 keV in orange, and 2.2–2.7 keV in purple energy photons in order to represent the total observed intensity including Ne, Mg, Si, and S lines, respectively. The X-ray contour levels are overlaid on the color-coded adaptively smoothed images. The green structure represents the radio emission at 843 MHz. The abundance distribution asymmetries and inhomogeneities are evident.

5. Results and discussion

The archival Suzaku data of G290.1-0.8 were analyzed in order to define the heavy element distribution within the vicinity. The SNR is located in a very dense portion of the gamma-ray sky as shown in Figure 1. Based on the gamma-ray analysis, the emission is best described by a hadronic model [12]. G290.1-0.8 plasma is very rich in heavy elements as clearly seen by the raw source spectra in Figure 2, right panel.

The SNR has a center-filled X-ray and shell-like radio structure, which classifies it as a mixed-morphology SNR (Figure 3). The radial X-ray spectra are modeled with a relatively homogenous thermal plasma of kT∼0.5

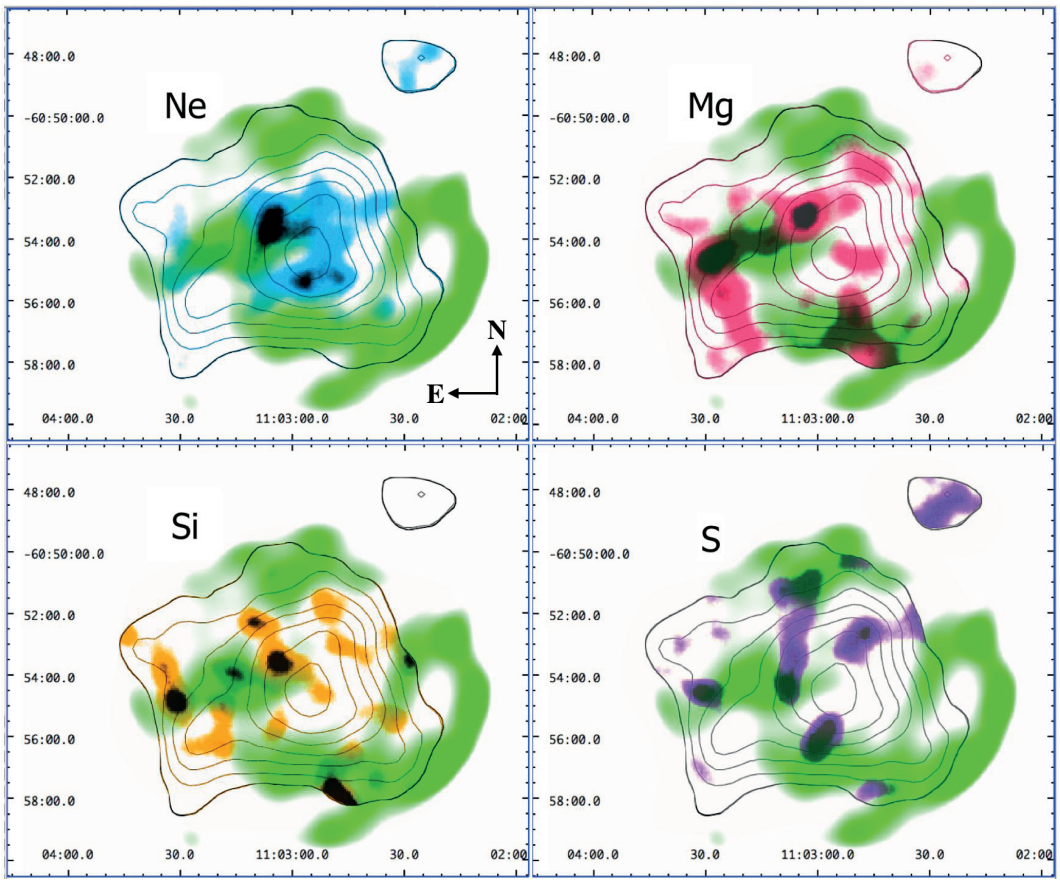

Figure 6. EW images for the elemental species Ne (0.89–1.10 keV), Mg (1.20–1.49 keV), Si (1.6–2.0 keV), and S (2.2–2.7 keV). The false colors are in units of eV for the EW maps and are in units of counts pixel^{-1}. The X-ray contours and radio plasma (in green) are overlaid in each image for visual aid.

keV and additional nonthermal origin with a photon index between 1.8 and 3.0 (Table 1). We further investigated the radial abundance distribution for Ne/Si, Mg/Si and S/Si, and found that the pattern can be described by the nucleosynthesis yield of core-collapse progenitor stars with a mass of 20∼25 $M_{\odot}$ (Figure 5). A similar finding was reported only for the NW plasma [11].

We presented EW maps for the elemental abundances of Ne, Mg, Si, and S (Figure 6), which allows us to determine the regions of enhanced metallicity in the SNR. The spatial distribution of the elemental abundances are shown in the EW maps for Ne, Mg, Si, and S (Figure 6). The maps show asymmetrical inhomogeneities, which is inherently usual in supernova explosions. In some SNR, the emission traces the ejecta distribution (as in the case of Cas A [26] and G292.0+1.8 [25]), and in some others, the emission is dominated by interstellar material (as in the case of PKS 1209-51, CTB 109, and Puppis A [27]. The northeast of the SNR G290.1-0.8 is bright in Ne, Mg, and Si. Mg and Si images look very similar. An arclike feature has been observed in the Si EW map of the SNR N40 and described as the edge of hot plasma reheated by reverse shock [28]. Similarly, as in the case of IC 443, the Si arc structure is interpreted to support the scenario of an intense reverse shock, propagating back into the remnant [29]. There is a clump in the east of Si and Mg map in this work (bottom-left in Figure 6) located on the edge of the X-ray contour elongation, which strengthens the hypothesis of a possible reverse shock.

Table 2. Energies of X-ray emission lines for Ne, Mg, Si and S.

Elements	Energy [eV]
Ne Kα.....	848.6
Mg Kα.....	1,253.6
Si Kα_1.....	1,739.4
Si Kα_2.....	1,740.0
S Kα_2.....	2,306.6
S Kα_1.....	2,307.8

The EW maps are enhanced in a slight elongation in the same (east to northwest) direction with the X-ray brightness contours, suggesting that these distorted X-ray structures are dominated by the ejecta. Recently, the ejecta asymmetries were systematically measured for 18 galactic SNRs to understand the complex X-ray morphologies [30]. The study concluded that neutron stars, formed in some core-collapse SN explosions, are preferentially moving opposite to the bulk of the X-ray emission, supporting the hydrodynamic-kick scenario [31]. Although there is no reported point-like object as a neutron star associated with G290.1-0.8, a supersonically traveling source ICG J11014-6103 was reported at the southwest of the SNR [15], which is a bit far (7 ± 1 kpc [8]) to describe a relation conclusively. In the literature, there are distant ($>$10 arcmin) neutron stars associated with SNR asymmetries such as W44 and MSH 15-56 [30]. However, one cannot totally exclude a similar scenario for G290.1-0.8. Based on the analysis results of this work, we conclude that the asymmetric ejecta, which is dominated by a core-collapse $20\sim25$ $M_\odot$ progenitor star, is associated with an undetected neutron star at the southwest, unless ICG J11014-6103 is related to the main body SNR.

Acknowledgments

We are grateful to the anonymous referee for their helpful comments and suggestions that improved the quality of the paper. We thank all members of the Suzaku operation and calibration teams. We also would like to acknowledge the support from the YTU Office of Scientific Research Project Coordination (BAP) funding with the contract number FYL-2018-3309.

References

[1] Seward, F. D. *Comments on Astrophysics* **1985**, *11*, 15-51.

[2] Rho, J.; Petre, R. *Astrophys. J.* **1998**, *503*, L167-L170.

[3] Slane, P.; Smith, R. K.; Hughes, J. P.; Petre, R. *Astrophys. J.* **2002**, *564*, 284-290.

[4] Mills, B. Y.; Slee, O. B.; Hill, E. R. *Aust. J. Phys.* **1961**, *14*, 497-507.

[5] Kirshner, R. P.; Winkler, P. F. Jr. *Astrophys. J.* **1979**, *227*, 853-855.

[6] Kesteven, M. J.; Caswell, J. L. *Astron. Astrophys.* **1987**, *183*, 118-128.

[7] Milne D. K.; Caswell J. L.; Kesteven M. J.; Haynes R. F.; Roger R. S. *Proceedings of the Astronomical Society of Australia* **1989**, *8*, 187-194.

[8] Reynoso, E. M.; Johnston, S.; Green, A. J.; Koribalski, B. S. *Mon. Not. R. Astron. Soc.* **2006**, *369*, 416-424.

[9] Seward, F. D. *Astrophys. J. Suppl. S.* **1990**, *73*, 781-819.

[10] Garcia, F.; Combi, J. A.; Albacete-Colombo, J. F.; Romero, G. E.; Bocchino, F.; Lopez-Santiago, J. *Astron. Astrophys.* **2012**, *546*, 91-99.

[11] Kamitsukasa, F.; Koyama, K.; Uchida, H.; Nakajima, H.; Hayashida, K.; Mori, K.; Katsuda, S.; Tsunemi, H. *Publ. Astron. Soc. Jpn.* **2015**, *67*, 1-8.

[12] Auchettl, K.; Slane, P.; Castro, D.; Foster, A. R.; Smith, R. K. *Astrophys. J.* **2015**, *810*, 43, 1-12.

[13] Yamaguchi, H.; Tanaka, M.; Maeda, K.; Slane, P. O.; Foster, A.; Smith, R. K.; Katsuda, S.; Yoshii, R. *Astrophys. J.* **2012**, *749*, 137-146.

[14] Atwood, W. B.; Abdo, A. A.; Ackermann, M.; Althouse, W.; Anderson, B.; Axelsson, M.; Baldini, L.; Ballet, J.; Band, D. L.; Barbiellini, G. et al. *Astrophys. J.* **2009**, *697*, 1071-1102.

[15] Pavan, L.; Bordas, P.; P hlhofer, G.; Filipovic, M. D.; De Horta, A.; O'Brien, A.; Balbo, M.; Walter, R.; Bozzo, E.; Ferrigno, C. et al. *Astron. Astrophys.* **2014**, *562*, 122-130.

[16] Auchettl, K.; Ng, C.-Y.; Wong, B. T. T.; Lopez, Laura; Slane, P. *Astrophys. J.* **2017**, *847*, 2-20.

[17] Koyama, K.; Hyodo, Y.; Inui, T.; Nakajima, H.; Matsumoto, H.; Tsuru, T. G.; Takahashi, T.; Maeda, Y.; Yamazaki, N. Y.; Murakami, H. et al. *Publ. Astron. Soc. Jpn.* **2007**, *59*, 245-255.

[18] Whiteoak, J. B. Z.; Green, A. J. *Astron Astrophys* **1996**, *118*, 329-380.

[19] Ishisaki, Y.; Maeda, Y.; Fujimoto, R.; Ozaki, M.; Ebisawa, K.; Takahashi, T.; Ueda, Y.; Ogasaka, Y.; Ptak, A.; Mukai, K. et al. *Publ. Astron. Soc. Jpn.* **2007**, *59*, 113-132.

[20] Arnaud, K. A. *Astr. Soc. P.* **1996**, *101*, 17-20.

[21] Wilms, J.; Allen, A.; McCray, R. *Astrophys. J.* **2000**, *542*, 914-924.

[22] Yasumi, M.; Nobukawa, M.; Nakashima, S.; Uchida, H.; Sugawara, R.; Tsuru, T. G.; Tanaka, T.; Koyama, K. *Publ. Astron. Soc. Jpn.* **2014**, *66*, 68-77.

[23] Woosley, S. E.; Weaver, T. A. *Astrophys. J.* **1995**, *101*, 181-235.

[24] Sarazin, C. L. *X-ray Emission from Cluster of Galaxies*; Cambridge University Press: Cambridge, UK, 1988.

[25] Park, S.; Roming, P. W. A.; Hughes, J. P.; Slane, P. O.; Burrows, D. N.; Garmire, G. P.; Nousek, J. A. *Astrophys. J.* **2002**, *564*, L39-L43.

[26] Hwang, U.; Laming, J. M. *Astrophys. J.* **2012**, *746*, 130-148.

[27] Hwang, U.; Petre, R.; Flanagan, K. A. *Astrophys. J.* **2008**, *676*, 378-389.

[28] Park, S.; Burrows, D. N.; Garmire, G. P.; Nousek, J. A.; Hughes, J. P.; Williams, R. M. *Astrophys. J.* **2003**, *586*, 210-223.

[29] Troja, E.; Bocchino, F.; Miceli, M.; Reale, F. *Astron. Astrophys.* **2008**, *485*, 777-785.

[30] Holland-Ashford, T.; Lopez, L. A.; Auchettl, K.; Temim, T.; Ramirez-Ruiz, E. *Astrophys. J.* **2017**, *844*, 84-100.

[31] Wongwathanarat, A.; Janka, H.-Th.; Müller, E. *Astron. Astrophys.* **2013**, *552*, 126-151.